AN ABSTRACT OF THE THESIS OF

David William Rinaldi for the degree of Master of Science in Nuclear Engineering
presented on June 7, 2016.
Title: Radiation Detection Using a Semiconducting Nanocrystal Detector

Abstract approved: _____

Haori Yang

Nanostructured material has been projected to be the next generation material for the detection of ionizing radiation due to the uniquely superior physical processes associated with charge creation and by virtue of their optoelectronic tunablility. Semiconducting Nanocrystal (NC) detectors, by nature of their low band gap material, low fabrication costs, high densities, and direct radiation-to-charge formation (unlike scintillators) are poised to capture the best resolution of all NC radiation detectors. If adequately developed, semiconducting NC detectors could have a substantial impact in all areas where radiation spectroscopy is needed. Proof of concept detectors were shown to achieve resolution comparable to that of High Purity Germanium (HPGe) while operating at room temperature. However, all deposition processes performed (drop casting, spin casting, dip casting) even with various treatments (layer-by-layer treatment, ligand exchange, addition of a conductive polymer) have resulted in a material with structural defects and inhomogeneities which in turn create poor conditions for the mitigation of charge carriers, and ultimately thicknesses for the active detection medium have not surpassed the millimeter scale. In this thesis, a variety of Lead Selenide (PbSe) NC based radiation detectors were fabricated using a chemical synthesis and drop-cast deposition method, however, none were able to show sensitivity to radiation due to a low signal to noise ratio.

©Copyright by David William Rinaldi

June 7, 2016

All Rights Reserved

Radiation Detection using a Semiconducting Nanocrystal Detector

by

David William Rinaldi

A THESIS

submitted to

Oregon State University

in partial fulfillment of
the requirements for the
degree of

Master of Science

Presented June 7, 2016
Commencement June 2016

Master of Science thesis of David William Rinaldi presented on June 7, 2016

APPROVED:

Major Professor, representing Nuclear Engineering

Head of the School of Nuclear Science and Engineering

Dean of the Graduate School

I understand that my thesis will become part of the permanent collection of Oregon State University libraries. My signature below authorizes release of my thesis to any reader upon request.

David William Rinaldi, Author

ACKNOWLEDGEMENTS

This thesis has been constructed from the inherited science which has been built up and passed down by those who have come before me. On this note I must thank my adviser Dr. Haori Yang for his leadership, appropriating direction and freedom, and never putting me down for my mistakes. I also wish to thank everyone listed in my bibliography.

For their help thought this process I would like to thank Jon King for help with gold evaporation, Dr. Matt Graham and Hiral Patel for their assistance with my absorption measurements, and Kristin Swetland for bumping up my 3D parts requests. I cannot forget my undergraduate assistant, Nancy Sinha, who was a pleasure to work with. I would also like to thank all those who have engaged with me in theoretical discussions regarding this work, specifically Dr. Graham, and to all those on my committee.

Lastly, I would not be here if it wasn't for my parents, who have and continue to give me support regardless of the path I choose. To them, William and Susan Rinaldi, I am forever indebted. I also thank my girlfriend Laura as well as my friends, who like Dr. Yang, have had to put up with me throughout my graduate career.

It takes a whole village to raise a child.
-Igbo and Yoruba (Nigeria) Proverb

TABLE OF CONTENTS

Page

1. INTRODUCTION 1

1.1. A few words on Radiation and Radiation detectors 1

1.2. Motivation 3

2. NANOCRYSTALS AS A DETECTION MEDIUM 5

2.1. Theoretical Models for PbSe NCs 7

2.2. Implications of Quantum Confinement 9

2.2.1 Carrier Multiplication 10

2.3. Previous Work using Nanostructures 13

2.3.1 Nanoscintillators 13
2.3.2 Semiconducting Nanowires and NCs 13

2.4. Choice of Lead Selenide (PbSe) 14

2.5. Simulation 16

2.6. Synthesis and Surface Chemistry 16

2.7. Modifications to Improve Charge Transport 19

2.7.1 Ligand Exchange 19
2.7.2 Addition of a Semiconducting Polymer 20

3. METHODS 21

3.1. Synthesis of PbSe Nanocrystals (NCs) 21

3.1.1 Hot Injection Method 21
3.1.2 Cleanup Process 22

3.2. Detector Fabrication 23

3.2.1 Gold electrode plating 26

4. RESULTS AND DISCUSSION 28

TABLE OF CONTENTS (Continued)

Page

4.1. TEM images 28

4.2. Absorption 28

4.3. Electronic Characterization 30

4.4. Response to Radiation 32

5. CONCLUSIONS 34

BIBLIOGRAPHY 36

APPENDICES 41

A APPENDIX 3D Time Independent Schrödinger Equation derivation 42

B APPENDIX 3D Particle in a Box derivation 44

C APPENDIX MCNPX Card 46

LIST OF FIGURES

Figure		Page
2.1	Density of states ranging from the continuum of states in a bulk semiconductor, to the sparse electronic states of a NC, to isolated states of a molecule/atom [16].	7
2.2	Band gaps of CdSe quantum wells, wires, and dots are plotted against the length of the confined dimension. The bulk band gap is noted E_g while the diameter of the CdSe exciton diameter is labeled d_b [21].	9
2.3	Size dependent absorption spectra of spherical PbSe NCs with average diameter ranging from 3.3 nm to 8.1 nm [22].	10
2.4	*a* Illustration of Impact ionization II. C stands for the conduction band and V stands for the valance band. *b* Illustration of AR where E_g is the energy of the band gap [23].	11
2.5	*a* Relaxation via longitudinal optical (LO) phonons in bulk PbSe. *b* CM via Impact Ionization which can be the dominant de-excitation path in NCs [27].	12
2.6	Common W values. Taken from [14] with data from [28].	12
2.7	Temperature dependence on PbSe NC band gap which is up to an order of magnitude smaller than the bulk temperature dependence [36].	15
2.8	Alpha particles (green tracks) being stopped inside the black rectangle which is the PbSe NC medium.	16
2.9	*A*. Dynamics of NC growth based on the La Mer model *B*. Illustration of the hot injection method [41].	18
2.10	Model of a 5nm rock-salt crystalline structure PbS NC with OA^- and OH^- ligands [43].	19
3.1	Experimental setup during the synthesis of PbSe NCs.	22
3.2	NC+ethanol solution after centrifuging. Note the NC on the walls of the tube and the ethanol ready to be decanted.	22
3.3	Class A prototypes. Left detector shows NC spotting with an arrow pointing towards damaged NCs. Detector on right has been plated with gold.	23

LIST OF FIGURES (Continued)

Figure		Page
3.4	Class B prototypes without electrode connections.	24
3.5	Testable class C prototypes with a ruler for scale.	25
3.6	Class D prototypes with their removed top electrodes.	25
3.7	Gold evaporation machine in use. The intense heat of the boat causes illumination.	26
4.1	TEM image of 7-12 nm spherical PbSe NCs.	29
4.2	Leftmost vial is the stock PbSe batch 512, the middle cuvette is a concentrated dark sample and the rightmost cuvette is a diluted light sample.	29
4.3	Absorption curve over the 200-3,000 nm range.	30
4.4	Absorption curve highlighting the characteristics of the NCs at smaller wavelengths.	31
4.5	IV curve for four class C detectors	32
4.6	Mock setup of the detector and preamplifier configuration used in the radiation response testing.	33

LIST OF TABLES

Table		Page
2.1	Exciton, electron, and hole Bohr radii of typical NC semiconductors [15].	14
2.2	Different PbSe structures by changing key variables.	19

RADIATION DETECTION USING A SEMICONDUCTING NANOCRYSTAL DETECTOR

1. INTRODUCTION

1.1. A few words on Radiation and Radiation detectors

The term radiation can sometimes be vague and ambiguous. Merriam-Webster defines radiation as the process of emitting radiant energy in the form of waves or particles [1] allowing others to include acoustic radiation such as sound within this scope [2]. For the remainder of this thesis, the term radiation will be shorthand for ionizing radiation which includes any particle or electromagnetic wave capable of ionizing tightly bound electrons from an atom. Radiation detectors will be defined as any developed device which responds in some predictable, repeatable way to the presence of radiation.

Radiation detectors extend our view of the environment ultimately by some means of charge creation. Some forms of radiation such as alpha or beta particles are charged themselves, whereas charge-neutral particles such as photons (if considered as a particle) or neutrons must first have an interaction with matter to create charge, which can then relay information about the radiation. Some detectors such as scintillators operate by emitting light after interactions with radiation which is then converted to charge through an axillary piece of equipment such as a photomultiplier tube or a photo diode. These charges are usually sent through an electric circuit consisting of a pre-amplifier and amplifier before being analyzed.

Radiation detectors are usually classified by their mediums into three categories:

gas, scintillators, and semiconductors. One of the primary differences is the energy needed to liberate an ion pair (or electron-hole pair), which is two units of charge. The less energy needed to create charge, the more charge created per incident radiation, the more information can be deduced about the radiation. Although there are many types of radiation detectors in each category, by taking a look at popular representatives we can get some idea about the energy resolution of different detectors based on how much energy it takes to produce charge carriers in their detecting material. We see that air, a typical gas detector medium, requires about 34 electron volts (eV) per pair of charge [3]. Sodium iodine, a typical scintillator medium requires about 20 eV per pair [4] although charge is not generated within the scintillation material itself. A high purity germanium (HPGe) semiconducting crystal has a band gap of 0.7 eV [5], and needs about three times this energy to liberate an electron hole pair-as long as the germanium crystal is typically kept below 110 K. Currently, the state of the art room temperature semiconducting detector is cadmium zinc telluride (CdZnTe aka CZT) which has a band gap of 1.6 eV [6] and also needs about three times this value to produce charge carriers. Thus, semiconducting radiation detectors are known to have the best energy resolution due to their ability to generate and collect much larger amounts of information per incident radiation. However they are usually the most expensive and in some instances, such as with the high purity germanium, require the active medium to be kept well below room temperatures.

In this thesis I will discuss my process of creating and testing nanocrystal (NC) radiation detectors. Starting with the theoretical advantages of nanocrystals over classical mediums (2., 2.2.1) I will summarize some previous work (2.3.), discuss a simulation of a bulk PbSe detector (2.5.), and delve into the theory behind the synthesis (2.6.). Then I will move on the the physical process of fabrication and testing in Chapter 3. This will include the synthesis (3.1.) and characterization of the Lead Selenide (PbSe) NCs as well as the detectors response to radiation (4.4.). Thus, in this thesis, I describe how a radiation detector will be created from scratch to be evaluated and tested.

1.2. Motivation

The demand to detect, identify, and characterize radionuclides has steadily increased alongside the increasing employment of radionuclides in the food [7], medical [8], energy, as well as other industries. Further, radiation detectors play a pivotal role in strengthening homeland security as well as the international safeguards of nuclear weapons. Ultimately, the most desirable radiation detector is one that is 1) inexpensive 2) can be made to be a variable size (scalability) 3) has high intrinsic efficiency and high resolution. Thus far, no one technology is thought of having all three attributes. Of the main classes of detectors, gas filled detectors, are inexpensive but do not have high intrinsic efficiency nor high resolution. Scintillators are relatively expensive, some of which can be made to a variable size, and have average efficiency and resolution. Classical semiconducting detectors are by far the most expensive, are usually limited in size, but have desirable efficiency and resolution. Thus, it remains as a scientific endeavor to produce a material or method capable of meeting all the demands of an ideal detector which would find widespread utilization.

Nanocrystals (NCs) are particles which have at least one dimension less than 100 nm, and can also be classified as "Quantum Dots" (QDs) if the particles are semiconducting and are usually smaller, on the order of 2-10 nm [9]. Here we will refer to QDs as NCs and use the terms interchangeably. NCs have been of scientific interest for their potential application in thin film electronics [10], solar cells [11], biological sensors [12], and beyond. Attributes which have spawned this popularity include improved quantum efficiencies due to multiple exciton generation (MEG), the suppression of electron-phonon relaxation as well as having size, shape, and optoelectronic tunability. NCs are also complimented by low cost synthesis methods, specifically PbSe nanocrystals by a hot injection method reported by Murray and coworkers [13].

Semiconducting NC detectors, by nature of their low band gap material, high densities, and direct radiation-to-charge formation (unlike scintillators) are poised to capture the best resolution of all NC radiation detectors. If adequately developed, semiconducting NC detectors could have a substantial impact in all areas where radiation spectroscopy is needed. Proof of concept detectors were shown to achieve high purity germanium resolution while operating at room temperature by Kim [14]. However, all deposition processes performed (drop casting, spin casting, dip casting) even with various treatments (layer-by-layer treatment, ligand exchange, addition of a conductive polymer) have resulted in a material with structural defects and inhomogeneities which in turn create poor conditions for the mitigation of charge carriers, and ultimately thicknesses have not surpassed the millimeter scale. This work aims to recreate similar high resolution detectors from PbSe nanocrystals made from wet synthesis chemical methods which have thicknesses on the millimeter scale.

2. NANOCRYSTALS AS A DETECTION MEDIUM

Nanostructured material has been projected to be the next generation material for the detection of ionizing radiation due to the uniquely superior physical processes associated with charge creation and the simple tunability of the size and shape of the nanostructures themselves (not achievable in classical single crystal detectors) by means of high-quality, narrow size distributed, low-cost synthesis methods. The divergent properties which separates nanostructures, such as nanocrystals (aka Quantum Dots) from their classical counterparts are largely due to their discrete electronic states. Both bulk (classical) and nanocrystal based semiconductors adhere to the band theory of solids which outlines how electrons populate energy levels. Electrons populate the valance band which is the highest occupied energy level at 0 K, however, if given enough energy to surmount the band gap, the forbidden region in which electrons cannot exist, electrons will populate the conduction band, leaving behind a hole (an absence of an electron) in the valence band. Electrons in the conduction band are free to be influenced by external potentials where they become mobilized and generate current. Holes in the valance band are considered positive charge carriers as electrons in the valance band fill the hole left behind by the previous electron in the conduction band mimics the physics of a positive charge moving in the opposite direction. Together, an electron and a hole bound in their lowest energy state, commonly referred to as an electron-hole pair, can be modeled and classified as a quasi-particle called an *exciton*. Excitons have a finite size which is material dependent and is denoted as its Bohr exciton radius,

$$a_B = \frac{4\pi\epsilon(\infty)\hbar^2}{e^2}\left(\frac{1}{m_e} + \frac{1}{m_h}\right)$$

. Electrons and holes also have Bohr radii, each given by

$$a_{h,e} = \frac{4\pi\epsilon(\infty)\hbar^2}{m_{h,e}e^2}$$

Where $\epsilon(\infty)$ is the optical frequency dielectric constant, and $m_{h,e}$ are the hole/electron effective masses, $\hbar$ is the reduced Planck's constant and e is the elementary charge. If the size of the nanocrystal, denoted by its radius, R, is smaller or on the order of a_B, then physics of the *quantum confinement* regime becomes emergent. Moreover, the ratio of $\frac{R}{a_B}$ determines strong, intermediate, or weak confinement, with strong confinement corresponding to a lower ratio. In weak confinement, $R> a_{h,e}$, the electron-hole pair is mediated mostly by the Coulomb interaction. In intermediate confinement, $a_e > R > a_h$, the electron becomes quantized and becomes more energetic [15], however the hole which is not confined still is attracted to the electron under the Coulomb force. Only during strong confinement, $a_{h,e} > R$, can the Coulomb attraction be ignored as confinement energy imparted to the exciton becomes quite large. The most outstanding consequence of strong quantum confinement (or simply confinement for the remainder of the thesis), is the discretization of the NCs electronic states. Thus, NCs are sometimes called "artificial atoms" because their sparse electronic structure consisting of widely separated electron and hole energy states resembles that of isolated atoms and molecules as shown below in Figure 2.1. There, HOMO stands for Highest Occupied Molecular Orbital and LUMO stands for Lowest Unoccupied Molecular Orbital. This quantization resulting from strong confinement separates nanocrystal semiconductors from bulk semiconductors which have a continuum of energy levels in the conduction and valance bands. The topic of surface states will be touched on in later sections covering surface chemistry.

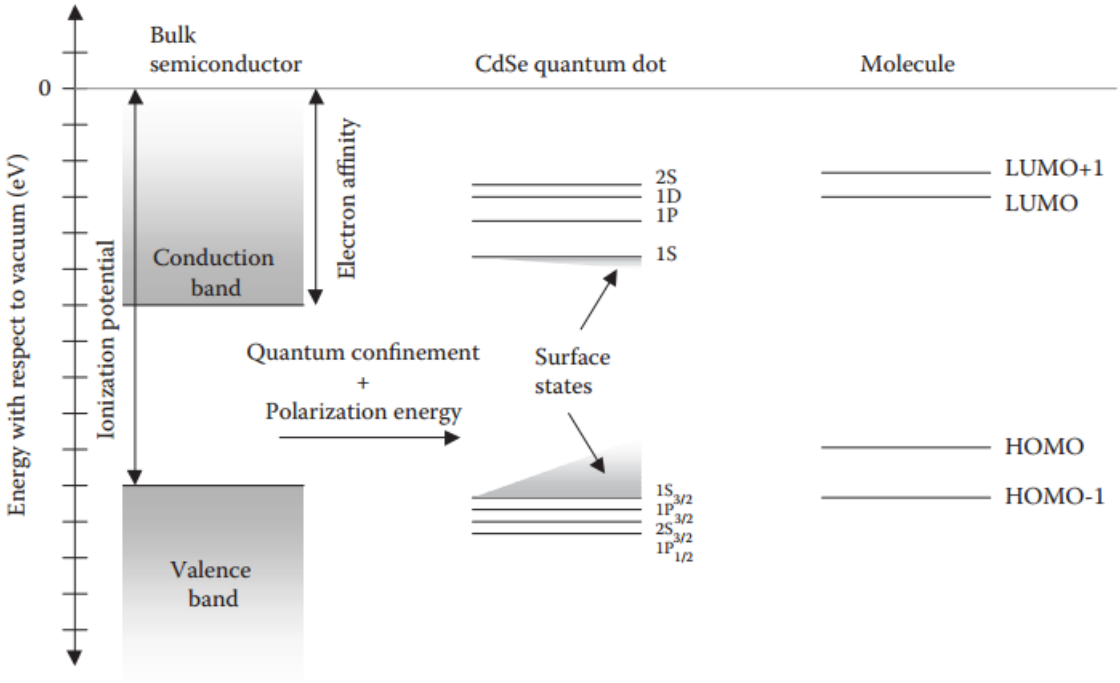

FIGURE 2.1: Density of states ranging from the continuum of states in a bulk semiconductor, to the sparse electronic states of a NC, to isolated states of a molecule/atom [16].

2.1. Theoretical Models for PbSe NCs

Simply put, there remains much interest and difficulty in the complete modeling of PbSe's electronic structure [17]. There has been success from using an envelope function, most notably by Kang and Wise [18], and a tight binding approximation [19], however they both cannot completely model the electronic and optical states of PbSe NCs. Perhaps the most simplistic approach which gleams light onto quantum confinement is the so called top-to-bottom particle in a box approximation. This method essentially treats either the hole or electron as a wave in a box where the potential remains at zero within the box and is infinite at the box's walls. This is a common introductory quantum mechanics problem

and its result is that only certain standing waves

$$\psi(x,y,z) = \psi_x(x)\psi_y(y)\psi_z(z) = \sqrt{\frac{8}{L_xL_yL_z}}sin(\kappa_x x)sin(\kappa_y y)sin(\kappa_z z) \tag{2.1}$$

$$\kappa_i = \frac{n\pi}{L_i}, i = x, y, z$$

with discrete energies

$$E_i = \frac{\kappa_i^2\hbar^2}{2m} = \frac{n^2\pi^2\hbar^2}{2mL_i^2} \tag{2.2}$$

which are based on the dimensions of the box ($L_i = L_x, L_y, L_z$), are suitable solutions. A derivation is shown in Appendix A and B. A more complex and accurate model could be developed by assuming a particle in a sphere with only a finite barrier at its surface, where one would incorporate spherical harmonics [14]. Both models result in the $1/L^2$ relationship between the size of the nanocrystal and the energy of the band gap, however, by empirical curve fitting and via more rigorous calculations, there is a stronger $1/L$ dependence on the NC band gap. A typical equation that models the PbSe NC band gap as a function of NC diameter is

$$E_0 = 0.278 + \frac{1}{0.016D^2 + 0.209D + 0.45} \tag{2.3}$$

where E_0 is the energy of the band gap in electron volts and D, the diameter of the nanocrystal is measured in nanometers [20]. Thus as the NCs become smaller, their band gap energies become larger, deviating from the horizontal asymptote which is the band gap of the bulk material, shown below in Figure 2.2

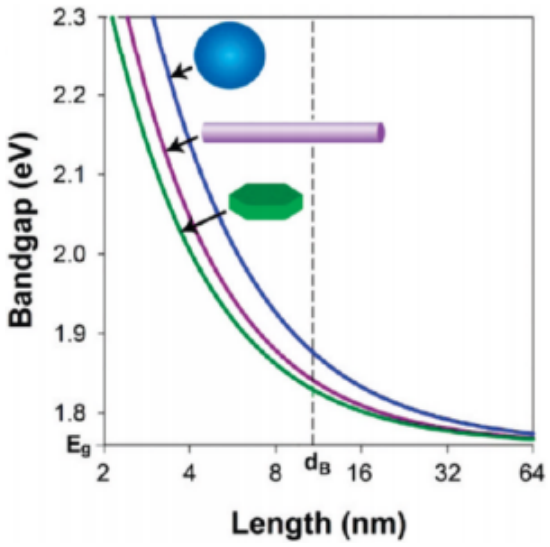

FIGURE 2.2: Band gaps of CdSe quantum wells, wires, and dots are plotted against the length of the confined dimension. The bulk band gap is noted E_g while the diameter of the CdSe exciton diameter is labeled d_b [21].

As a note on confinement and the objects in Figure 2.2, nanocrystals are thought to be a zero dimensional object since they exhibit confinement in all three dimensions. Nanowires are one dimensional objects since they exhibit confinement in two dimensions and quantum wells are two dimensional objects with confinement in only one dimension.

2.2. Implications of Quantum Confinement

The tunable size and shape of the nanocrystal has direct effects on the resulting band gap, most importantly, the smaller the dimension of confinement, the larger the band gap. The size of the band gap results in different absorption and emission spectra. This is most apparent when a hole in the valance band and and electron from the bottom of the conduction band go through *recombination*, and release a photon with an energy equal to the band gap.

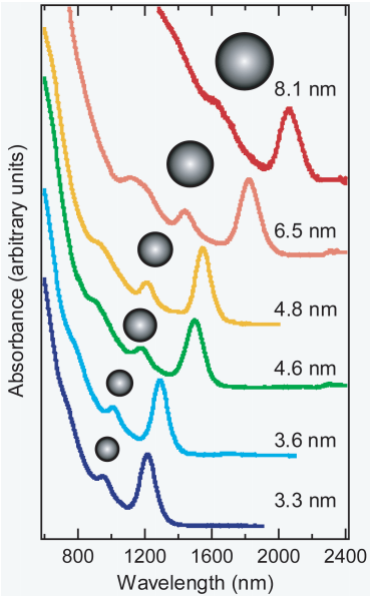

FIGURE 2.3: Size dependent absorption spectra of spherical PbSe NCs with average diameter ranging from 3.3 nm to 8.1 nm [22].

2.2.1 Carrier Multiplication

Carrier Multiplication (CM) is the formation of more than one exciton produced per absorbed photon. The traditional mechanism for CM known as Impact Ionization (II) the reverse process of Auger Recombination (AR). AR is the process in which an exciton recombines and imparts its energy to an electron or hole which may stay or leave the NC. The reverse of AR involves an exciton, created by absorbing a photon of energy of at least $2E_g$, transferring at least $1E_g$ of excess energy to a valence band electron, which is then excited above the energy gap, before relaxing to the band edge [23]. Both II and AR are shown below in Figure 2.4.

CM has also been described under a theory called Multiple Exciton Generation (MEG) sometimes dubbed the coherent-CM model as it explains MEG a coherent evolution of the quantum state from the initial single exciton to a coherent superposition of multiple exciton states, however this theory faces debate [24, 25, 26].

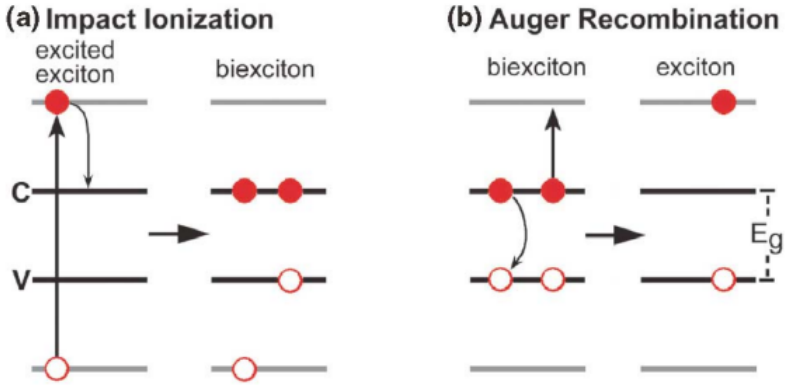

FIGURE 2.4: *a* Illustration of Impact ionization II. C stands for the conduction band and V stands for the valance band. *b* Illustration of AR where E_g is the energy of the band gap [23].

Competing with CM is a process known as electron cooling, phonon-assisted electron relaxation, phonon scattering, or simply phonon emission; all which can be thought of as heat loss. This is shown in Figure 2.5. Although this mechanism is dominant in bulk semiconductors, because of the discrete electronic states of a NC, the difference in energy between levels can be many times the typical phonon energy, forcing the emission of several simultaneous phonons which becomes more unlikely with the increasing numbers of phonons. This is aptly named a "phonon bottleneck". Moreover, NCs have an increased Coulomb interactions making AR and II more efficient. Coupled with less restriction on momentum conservation (NCs are so small that Heisenberg's uncertainty principle makes momentum an unusable quantum number), it has been shown that II becomes competitive with phonon scattering, especially with higher absorbed photon energies. However, CM can still occur with absorbed photons low as $2E_g$ which is the limit set by energy conservation [25].

Onto a macroscale, CM imparts a lower average ionization energy, also known as a W value, to its parent material. The W value, being the average amount of energy needed to create an ion pair specific to that material, is in essence a parameter which describes

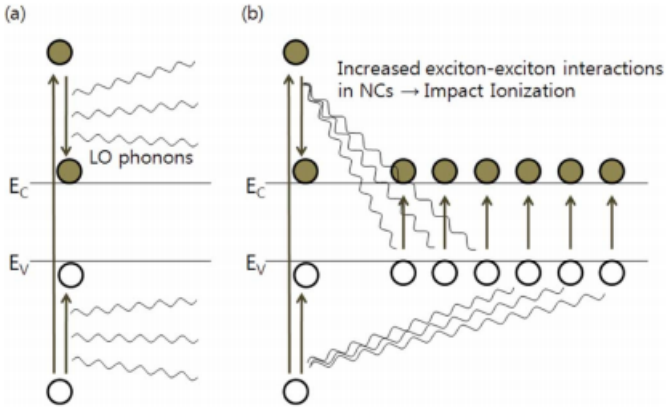

FIGURE 2.5: *a* Relaxation via longitudinal optical (LO) phonons in bulk PbSe. *b* CM via Impact Ionization which can be the dominant de-excitation path in NCs [27].

the amount of possible charge carriers and thus the resolution and efficiency of a detector made with that material. It is desired that the ratio of the W value to the materials band gap, E_g be unity, a limit imposed by the conservation of energy. Some common radiation detection material is shown in Figure 2.6.

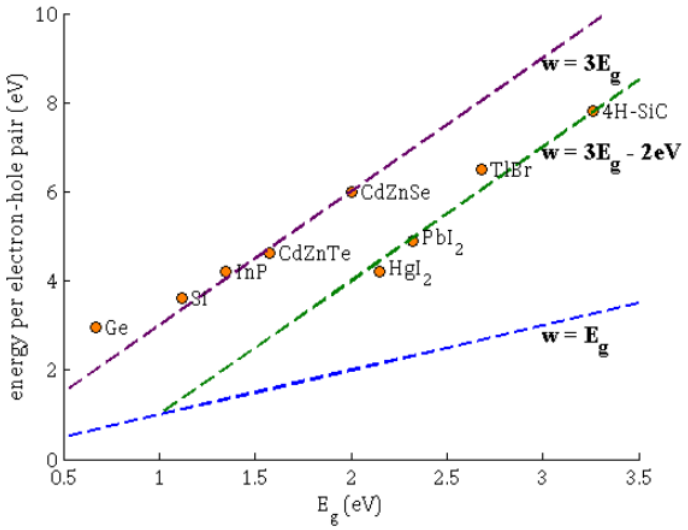

FIGURE 2.6: Common W values. Taken from [14] with data from [28].

2.3. Previous Work using Nanostructures

2.3.1 Nanoscintillators

Due to the lesser utilization of heat loss pathways as well as having a tunable radiative emission spectra, there is a strong push to incorporate NCs in radiation detectors as a scintillating material.

The experiments and arguments presented in [29] show that the use of nanocrystalline oxides as well as nanocrystalline lutetium and lanthanum fluorides for radiation detectors promote an increase in the light yield and sensitivity; accelerate the registration rate of ionizing radiation, and the increase in radiation hardness of the detectors. Other work investigating the use of fluoride nanoscintillators such as CaF_2:Eu, BaF_2:Ce, and LaF_3:Eu resulted in successful scintillation and the call for further investigation [30].

Work done at the University of Michigan [31] loading CeF_3 nanoparticles in an organic scintilating matrix was shown to be capable of detecting neutron capture γ-rays that cannot be detected using conventional BaF_2 scintillators. However, this came at a reduction of light yield which was determined to be caused by the Oleic Acid capping ligands by means of quenching detector luminescence, an effect which could be circumvented in the future via ligand exchange. In the same study was a proof of concept scintillator that was loaded with fissionable nanoparticles. The fissionable complex used, $Th(NO_3)_4(TBP)_2$ utilizing ^{232}Th, showed to have a higher response to x-rays than scintillator alone due the presence of high-Z material and proved that a detector loaded with fissionable nanoparticles could be used to detect neutrons.

2.3.2 Semiconducting Nanowires and NCs

Much focus has been on using Cadmium and Lead chalcogenides that is, nanocrystals which have a chemical formula of CdX or PbX where X is any member of the group 16 elements. Most popular include CdTe, CdSe, CdS, PbSe, PbS, and PbTe. Of these,

CdTe and PbSe are the most studied for radiation detection. Both have promise as high resolution radiation detectors which operate at room temperatures. CdTe and PbSe NC detectors as well as CdTe nanowire detectors were proven to show response to alpha particles as well as gamma rays [14].

2.4. Choice of Lead Selenide (PbSe)

As a II-VI semiconducting material CdTe has many attractive properties, including an absorption/emission spectrum which is mostly in the visible range and benefits from a more characterized synthesis method, stemming from their study as exceptional biological markers and utility in solar cells [32]. However, the IV-VI semiconducting PbSe boasts a large exciton Bohr radius of 46 nm, translating to a very strong confinement regime $\frac{a_b}{R}$ [33] as opposed to others in Table 2.1. This is over 4 times the exciton radius of CdTe, which is around 15 nm [34].

TABLE 2.1: Exciton, electron, and hole Bohr radii of typical NC semiconductors [15].

	a_B (nm)	a_e (nm)	a_h (nm)
II-VI: CdSe	3	3	< 1
II-VI: CdS	2	2	< 1
III-V: InP	9	7	2
III-V: GaAs	10	8	1
IV-VI: PbS	20	10	10
IV-VI: PbSe	47	23	24

PbSe also importantly has shown to have a small temperature dependence associated with its band gap $\frac{dE_g}{dT}$ shown in Figure 2.7. This differs from the bulk material which experiences a larger lattice expansion. Beyond this, the density of PbSe (8.07 $\frac{g}{cm^3}$) is much larger than CdTe (7.45 $\frac{g}{cm^3}$) which lends itself to an improved intrinsic efficiency of

a resulting radiation detector. Furthermore, PbSe nanocrystals seem to be the standard for testing high quantum yield (QY), with results of 300% when excited at $4E_g$ [35] and 700% QY at 7.8 E_g; the latter being close to the ultimate limit allowed by energy conservation at that exciton wavelength [26]. This translates to an average number of 3 ground-state excitons produced per absorbed photon carrying the energy of four times the energy of the PbSe band gap and 7 ground-state excitons produced per absorbed photon carrying the energy of 7.8 times the energy of the PbSe band gap, respectively.

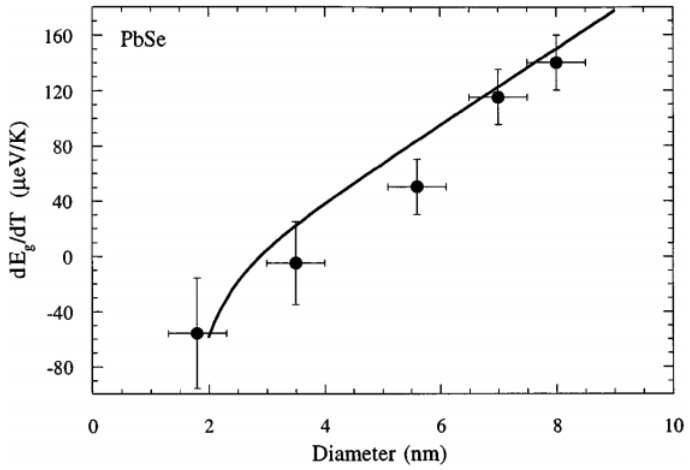

FIGURE 2.7: Temperature dependence on PbSe NC band gap which is up to an order of magnitude smaller than the bulk temperature dependence [36].

2.5. Simulation

The widely used Monte Carlo N-Particle Transport code MCNPX was used to model the detector and its response to alpha radiation for a qualitative understanding of how many alpha particles would be stopped within the detector. The alpha particles were emitted as a point source, each having an energy of 5.3 MeV to mimic the Polonium-210 source used in the lab. The PbSe medium was modeled as a right circular cylinder with a radius of 0.75 cm and a height of 1 mm. The capping ligands were not included due to their low density, low Z number, and hence low interaction with the alpha particles. The mixture which represented the detector medium was equal parts lead and selenium and was treated by MCNPX as a bulk solid. MCNPX Visual Editor was used to visualize the alpha particles transport through the detection medium and surrounding air, shown in Figure 2.8. The particles were preferentially biased upwards. As seen in Figure 2.8 most alpha particles are stopped within the detector. When the detector thickness was changed to a tenth of a millimeter the detector nonetheless stopped most alpha particles.

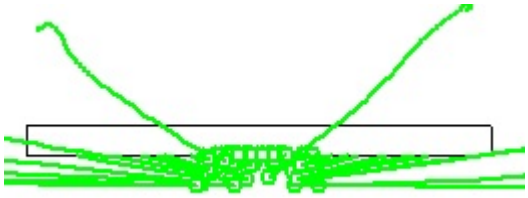

FIGURE 2.8: Alpha particles (green tracks) being stopped inside the black rectangle which is the PbSe NC medium.

2.6. Synthesis and Surface Chemistry

Most chemical synthesis methods of colloidal NCs rely on precursors, some surfactant, and a solvent. The term colloidal refers to the fact that the NCs are less than 1μm

in diameter and do not settle, or fall to the bottom of the liquid solvent they are contained in, but are uniformly suspended throughout it. At a certain critical temperature the precursors reach supersaturation, resulting in a burst of seed nucleation sites which lowers the concentration of the precursors in solution. After nucleation, the growth phase of the NCs begins and is heavily influenced by the surfactant molecules (also known as capping ligands), as well as the amount of time the NCs are allowed to grow, and the initial temperature of nucleation. This brief nucleation event and growth stage is outlined in the La Mer model [37] and is shown in Figure 2.9. During the growth stage a thermodynamically driven phenomena called Ostwald ripening occurs where smaller particles seem to dissolve while larger particles grow even larger. This occurs based on the fact that surface molecules are less energetically favorable than interior molecules, and since larger particles have a smaller surface area to volume ratio it is more desirable for a system comprised of larger particles. However, during this process, although the total number of particles decrease, and the average particle size increases, the total particle volume remains constant [38]. The capping ligands provide stabilization during the growth phase [39] and can be used to limit the growth rate of specific lattice planes during synthesis, changing the resulting geometric shape of the NC [40]. One synthesis method is to combine the precursors, surfactant and solvent in the same vessel and heat until nucleation [41]. The other, performed in this work, called the hot injection method or the high-temperature solution-phase route, involves heating the solvent and injecting a precursor/surfactant mix at a critical temperature. A variety of shapes of nanocrystal, and objects such as nanowires which requires the annealing of a multitude of NCs to form is shown in Figure 2.2.

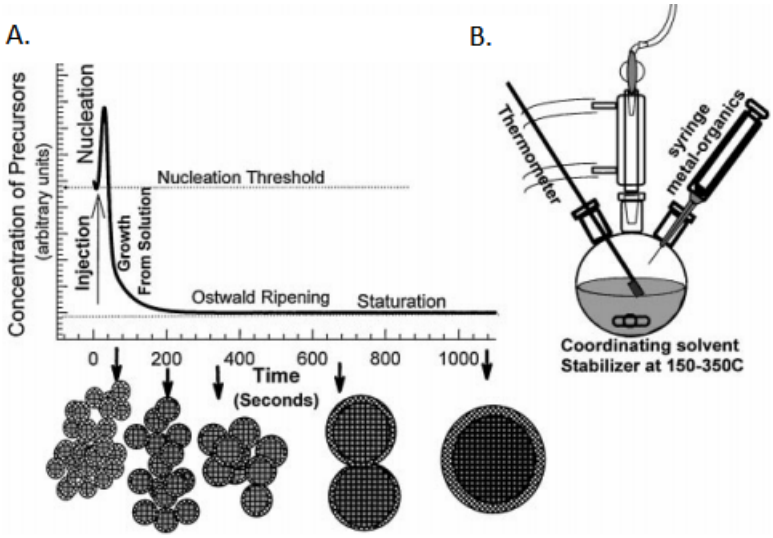

FIGURE 2.9: *A.* Dynamics of NC growth based on the La Mer model *B.* Illustration of the hot injection method [41].

In this work, the organic capping ligands used were Oleic Acid (OA). The ratio's used were not the same as in Figure 2.2 but instead closer to Pb:Se=1 and OA:Pb= 2.76. The temperature of injection and cooling were roughly the same however. While the NC core is responsible for many of the electronic and optical properties, the outer ligands are responsible for much of the NC's chemical properties. However, dangling surface bonds as well as capping ligands can alter the electronic states by creating charge carrier traps. The effect of surface states on the electronic structure are shown in figure 2.1. It has also been shown that when using TOPSe and $Pb(OA)_2$ as done here, over 90% of the ligands attached to the NC are OA and not TOP, with an average of about 4.2 OA ligands per square nanometer [40]. Figure 2.10 shows a model of a 5nm PbS NC with OA^- and OH^- ligands. This illustration gives a conceptual view of an NC with attached ligands which has the same rock-salt crystalline structure as PbSe.

TABLE 2.2: Different PbSe structures by changing key variables.

structure	stabilizing agents, solvent	OA:Pb ratio	Pb:Se ratio	injection/growth temperature (°C)	growth time
quasi-spherical nanocrystals	OA-TOP, Ph_2O, or OA-TOP, squalane	4:1	1:3	180/140−160	1−10 min
cubic nanocrystals	OA-TOP, Ph_2O	4:1	1:3	120/110[b]	5−15 min
octahedral nanocrystals	OA-DDA-TOP, Ph_2O	4:1	1:3	230/170	1−2 min
star-shape nanocrystals	OA-HDA-TOP, Ph_2O	4:1	1:3	230/170	2−5 min
undulated nanowires	OA-TOP, Ph_2O	3.15:1	3:1	250/170	1−5 min
zigzag nanowires	OA-HDA-TOP, Ph_2O	3.15:1	3:1	250/180	1−5 min
straight nanowires	OA-TDPA-TOP, Ph_2O	3.15:1	3:1	250/190	30 s−1 min
star-shape branched nanowires	OA-TOP, Ph_2O or OA-HDA-TOP, Ph_2O	3.15:1	3:1	250/170[b]	1−5 min
tapered branched nanowires ("nano-centipedes")	OA-HDA-TOP, octyl ether	3.15:1	3:1	250/170	1−3 min

OA, oleic acid; HDA, hexadecylamine; TOP, trioctylphosphine; Ph2O, phenyl ether; TDPA, n-tetradecylphosphonic acid. [b] Additional injections of Pb:Se precursors [42].

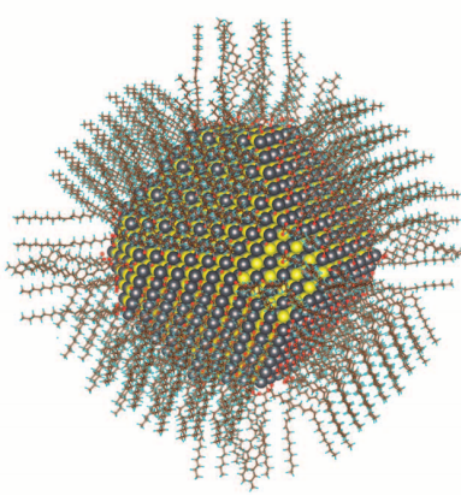

FIGURE 2.10: Model of a 5nm rock-salt crystalline structure PbS NC with OA^- and OH^- ligands [43].

2.7. Modifications to Improve Charge Transport

2.7.1 Ligand Exchange

Although very useful as a stabilizing agent, Oleic Acid (OA) does not have optimum charge transport properties. Thus, the removal of OA or another organic surfactant with replacement by a shorter chain ligand to allow better charge transport has become known

as ligand exchange [44]. Most common ligands include EDT and Hydrazine [45] made from layer-by-layer coatings. That is, every layer of deposited NCs is washed with a chemical compound to remove and replace the electrically insulating oleic acid molecules that originally solubilize the NCs [46]. Although not attempted in this work, Kim reports that when dried, the material contracts which leads to more cracking and deformation of the bulk material [14].

2.7.2 Addition of a Semiconducting Polymer

To aid in the extraction of charges created within the NC, the addition of an organic semiconducting polymer to the NCs material to make a blended structure has been attempted with success [14, 47]. The semiconducting polymer used in this work was MEH-PPV (Poly[2-methoxy-5-(2-ethylhexyloxy)-1,4-phenylenevinylene]). The addition of 30 or 60mg MEH-PPV in 2 mL chloroform was mixed with another 2 mL of NC+chloroform solution. This blended composite mixture was then deposited onto class C and D detectors outlined in Section 3.2.

3. METHODS

3.1. Synthesis of PbSe Nanocrystals (NCs)

3.1.1 Hot Injection Method

All chemicals used were purchased from Sigma-Aldrich with purities 97% and above, used without further purification. In a glovebox under inert conditions (argon) a two-neck flask was filled with 0.65 g Lead(II) acetate trihydrate ($Pb(CH_3COO)_2$), 8 mL trioctylphosphine (TOP), 1.5 mL OA, and 2 mL diphenyl ether (DPE). The flask was then transferred to the schlenk line with minimal oxygen exposure by means of crimping the gas tube which connects the chiller to the schlenk line. These reactants were heated via hot plate to 90°C for one hour under a fume hood while being degassed through a vacuum connected to the schlenk line. During this time, 1 molar trioctylphosphine selenium (1 M TOP-Se) was prepared by using 0.131 g of selenium powder thoroughly mixed with 1.7 mL TOP in glove box and then transferred into a 20 mL syringe. After the heated mixture cooled it was drawn into the same syringe as the 1 M TOP-Se. In a three-neck flask, 10 mL diphenyl ether (DPE) was heated to 150°C under a steady flow of argon . Magnetic stirrers were added and agitation was induced by a magnetic field from the hotplate, which was set to a maximum throughout the rest of the procedure to ensure the greatest yield of NCs. After temperature stabilization, the syringe containing all reactants was injected into the three-neck flask as the temperature dropped to roughly 100-110°C. As the temperature rose, effort was placed in trying to maintain the temperature around 130-140°C to enable growth of the NCs for roughly 6 minutes. Figure [**?**] shows a typical layout of the experimental setup. Directly after the growth period, the three-neck was placed into a large, cold, water reservoir where the temperature rapidly dropped off. After the solution was left to cool it was placed in vials in equal parts with ethanol. This usually

resulted in about 20-24 mL of uncleaned product.

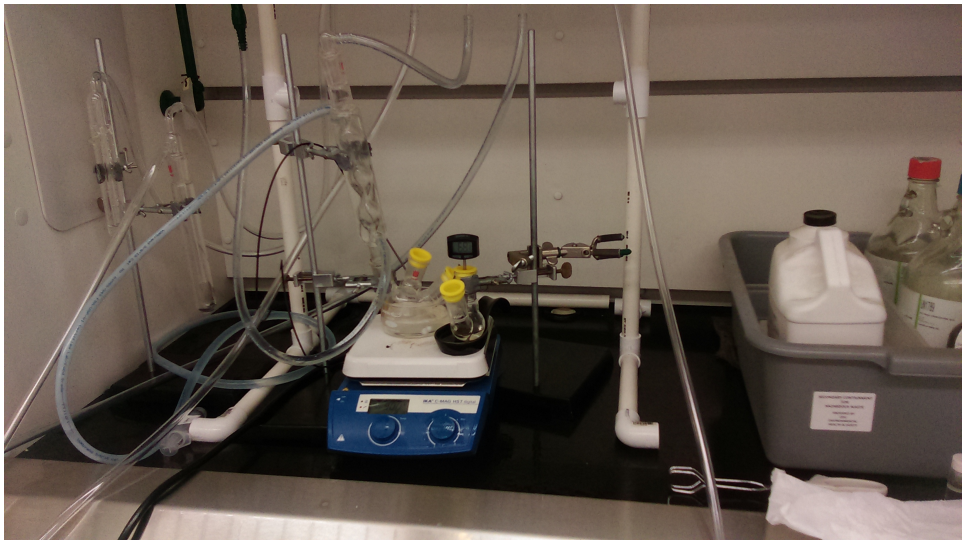

FIGURE 3.1: Experimental setup during the synthesis of PbSe NCs.

3.1.2 Cleanup Process

To remove any unreacted solvents and precursors, the vials containing equal parts ethanol and NC were centrifuged at 3,000 rpm for ∼1 minute. This caused the NCs to adhere to the walls of the vials allowing the supernatant to easily be decanted, shown below in Figure 3.2.

FIGURE 3.2: NC+ethanol solution after centrifuging. Note the NC on the walls of the tube and the ethanol ready to be decanted.

This process was repeated for a minimum of three times (or until the supernatant was clear) before the NCs were re-suspended in 1∼2 parts chloroform resulting in only a few mL (4∼6) of NCs mixed with chloroform. Glassware was scrubbed under water and later cleaned with aqua regia, a mixture of 1 parts nitric acid to 3 parts hydrochloric acid, to remove any excess heavy metals. The glassware was then rinsed with deionized water and with isopropyl alcohol and left to dry in a oven.

3.2. Detector Fabrication

All detectors were made via a drop casting method. Each drop was cast from a 25μL pipette onto a variety of detector housings. Qualitatively, the detectors were categorized into four classes A, B, C, and D. Class A were prototypes which were deposited onto a copper plate with no housing and thus was not able to achieve substantial thicknesses and was instead spread over the copper canvas. As seen in in Figure 3.3, detectors were of low quality due to their tendency to disperse over the surface of the copper.

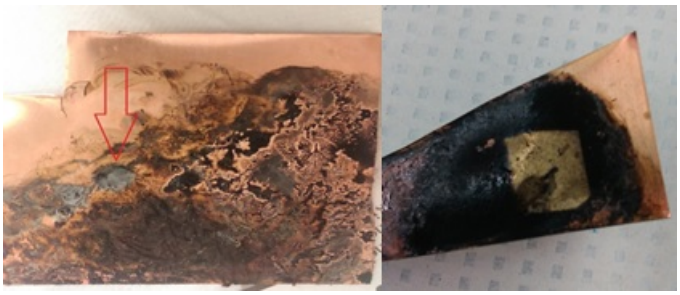

FIGURE 3.3: Class A prototypes. Left detector shows NC spotting with an arrow pointing towards damaged NCs. Detector on right has been plated with gold.

Class B prototypes solved this problem by structurally confining the NCs within a PLA 3d printed plastic housing, however, the thin sheets of aluminum which were cut and glued to their bottom which served as an electrode were difficult to mask and make an electrical connection to. None of the class B detectors were able to proceed to radiation

testing. Class B prototypes are pictured in Figure [**?**].

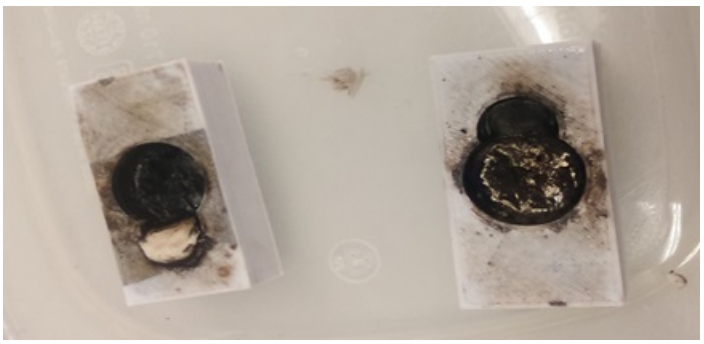

FIGURE 3.4: Class B prototypes without electrode connections.

Class C prototypes were a mixture of A and B prototypes, using a copper/aluminum bottom (also serving as an electrical contact) which a wire was easily soldered onto and also utilized a thin (2 mm) 3d printed PLA housing which was super-glued to the bottom electrode to confine the liquid NC solution. Some class C detectors were blended with ∼60mg of the MEH-PPV conductive polymer, such as the detector with the copper bottom in Figure 3.5 To make the top contacts, a silver based conducting epoxy was set onto the NC and cured with a wire embedded in it. Some class C detectors had electrodes made by soldering a wire to their tops. In this case, some of the PLA plastic melted along with the solder and the entire mix, in contact with the NC surface, allowed for a stable electrical connection proved by the I-V curves in Section 4.3.. Directly soldering a wire onto the NC surface proved to be a futile effort.

Finally, class D prototypes were created which were similar to class A detectors as they did not have any of the PLA plastic to contain the liquid NCs. Instead, a small indentation in the copper held the liquid to a central area. Since class C detectors did not respond well to radiation, class D detectors were purposefully made to be very thin. The indentation worked well for deposition, eliminating some of the problems of having the plastic housing such as having the NC solution mix with the glue underneath the plastic, however, the top electrodes all fell off as the conductive glue used did not adhere onto

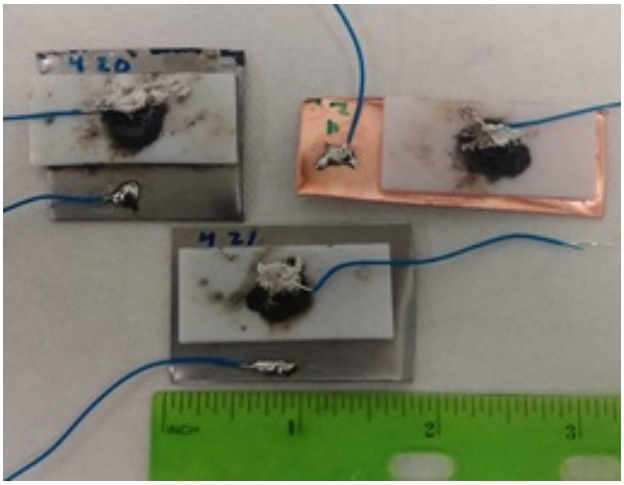

FIGURE 3.5: Testable class C prototypes with a ruler for scale.

the top surface of the NCs. All class D detectors had a mixture of ∼30 mg MEH-PPV and none were able to be tested for a response to radiation. Class D detectors are shown in Figure [**?**], with the top contacts disconnected after normal handling amputated their weak connection to the detectors.

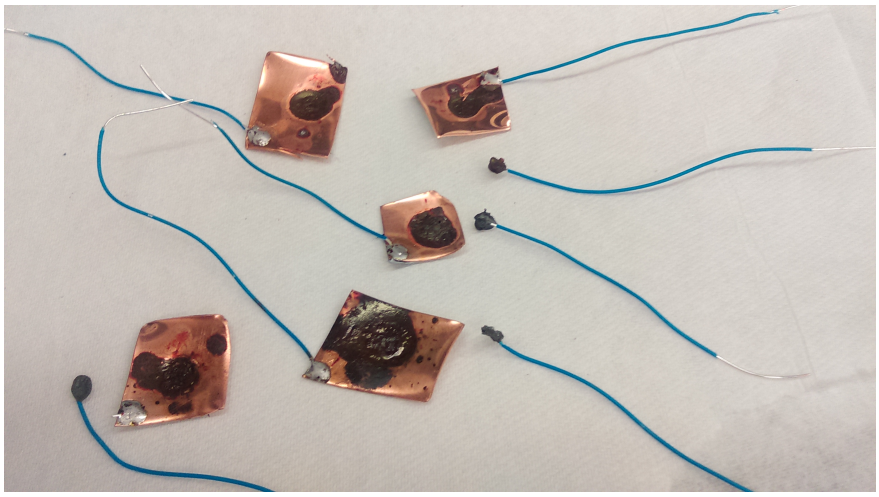

FIGURE 3.6: Class D prototypes with their removed top electrodes.

3.2.1 Gold electrode plating

Gold was evaporated using a Denton Vacuum gold evaporator. Trials used about 30-230 mg of high purity gold placed in a boat sealed by a glass dome as seen in Figure [**?**]. Pressure within the dome fell to about $8 \cdot 10^{-5}$ torr while about 78 A flowed through the boat, evaporating the gold resting on it. The gold particulates then rose and deposited onto the surface of the NCs as electrical tape masked the bottom contact from the gold. Overall, little success came from gold electrode plating as the non uniform surface required very large amounts of gold, upwards of 150 nm coatings which are usually adequate for plating smooth surfaces such as metals. Further, it would be still necessary to attach either a wire or have some sort of solid peace of metal connected to the gold by physical contact.

FIGURE 3.7: Gold evaporation machine in use. The intense heat of the boat causes illumination.

Thus, no detectors plated with gold (only two in total) ever completed electrical evaluation nor were tested for any response to radiation. It is possible that gold electrode plating could be a means of creating an electrical contact if one deposits a substantial amount of gold to the surface and connects the correct leads which can be connected to the resulting detection signal chain.

4. RESULTS AND DISCUSSION

4.1. TEM images

PbSe NCs suspended in chloroform were imaged by Oregon State University's Electron Microscopy facility using their Titan Transmission Electron Microscope (TEM). Samples were diluted and placed on a graphine oxide grid and were imaged at 450,000x resulting in clear images of individual NCs in small clusters as shown in Figure 4.1. The sharp parallel lines spaced about 0.2-0.4 nm represent the crystal's lattice planes, showing that the NCs exhibit a highly crystalline structure with an overall spherical shape. As seen here and later in Section 4.2 the size distribution is quite large as no size selection techniques were administered. Size selection techniques come at a cost of a reduction of NC yield while this work placed heavy emphasis on prototyping of as many detectors as possible.

4.2. Absorption

Absorption measurements were taken with a Cary 5 spectrophotometer through the Oregon State Physics Department. PbSe NCs suspended in chloroform held in quartz cuvettes were tested using variable dilutions as shown in Figure 4.2. Samples with higher concentration of PbSe are labeled as "dark" while the more dilute samples are labeled as "light"' in Figure 4.3and Figure 4.4.

Figure 4.3 shows the full absorption curves for two different dilutions of two different batches of PbSe. Each batch, labeled 420 and 512 (for their production dates) were both made under similar conditions. The solvent choloroform was run once on its own to help differentiate peaks from the solvent and the NCs. Interestingly, peaks from the solvent

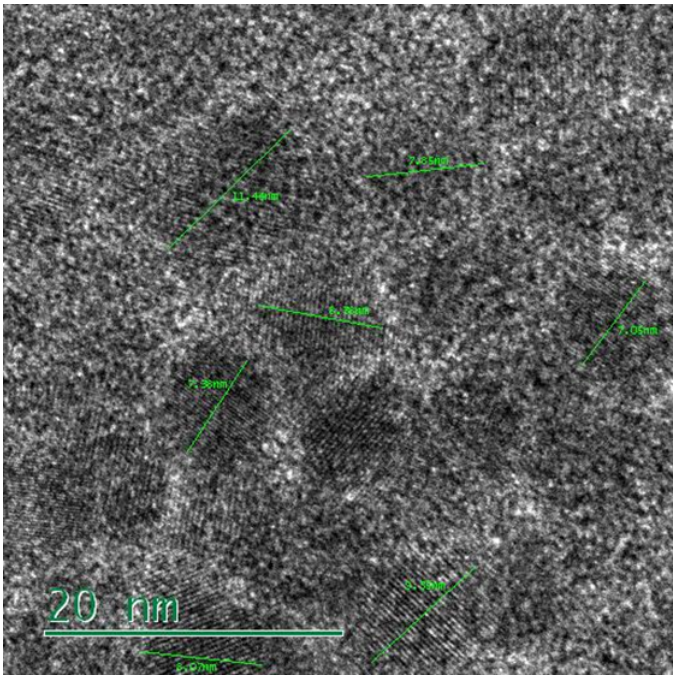

FIGURE 4.1: TEM image of 7-12 nm spherical PbSe NCs.

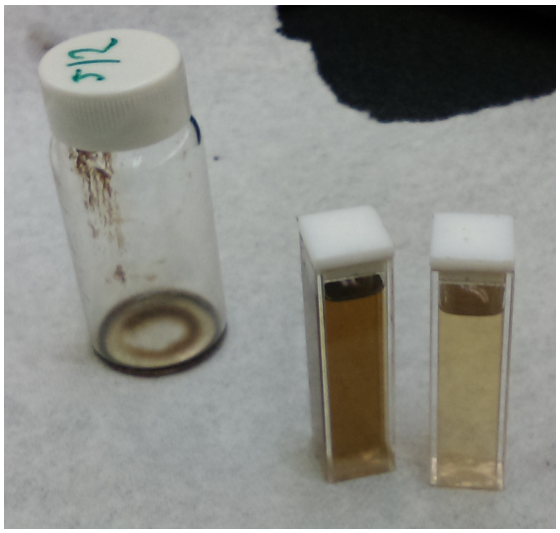

FIGURE 4.2: Leftmost vial is the stock PbSe batch 512, the middle cuvette is a concentrated dark sample and the rightmost cuvette is a diluted light sample.

were substantially amplified when mixed with the NCs. This is thought to be due to the aided scattering provided by the NCs which darken the sample and allow less light to pass

through to the detector. Besides this amplification, the spectra with NCs all followed the pure solvent sample closely until the lower wavelengths (∼1,000 nm) where the broad NC peaks make an appearance.

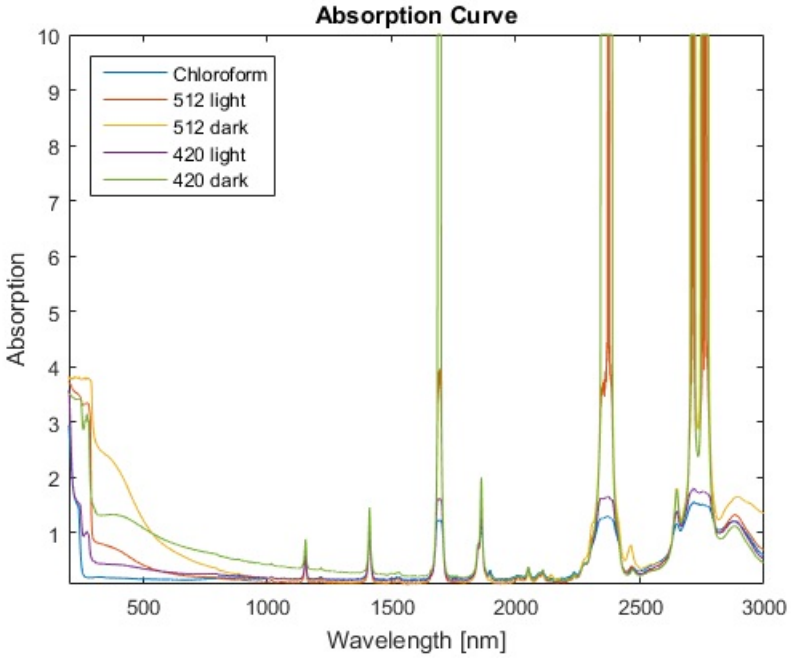

FIGURE 4.3: Absorption curve over the 200-3,000 nm range.

Looking at these lower wavelengths a bit closer in Figure 4.4 shows the unique departure from pure solvent. The two dilutions of the 420 sample seem to exibit the same traits with a similar hump at about 280 nm. Further, the concentrated 420 sample shows absorption all the way out to about 1500 nm.

4.3. Electronic Characterization

A Keysight B2901A Precision Source/Measure Unit was used to take a Current-Voltage sweep measurement, resulting in the generation of an I-V curve. The applied voltage across the detector ranged from -35-35 V with a total of 1,000 measurement steps

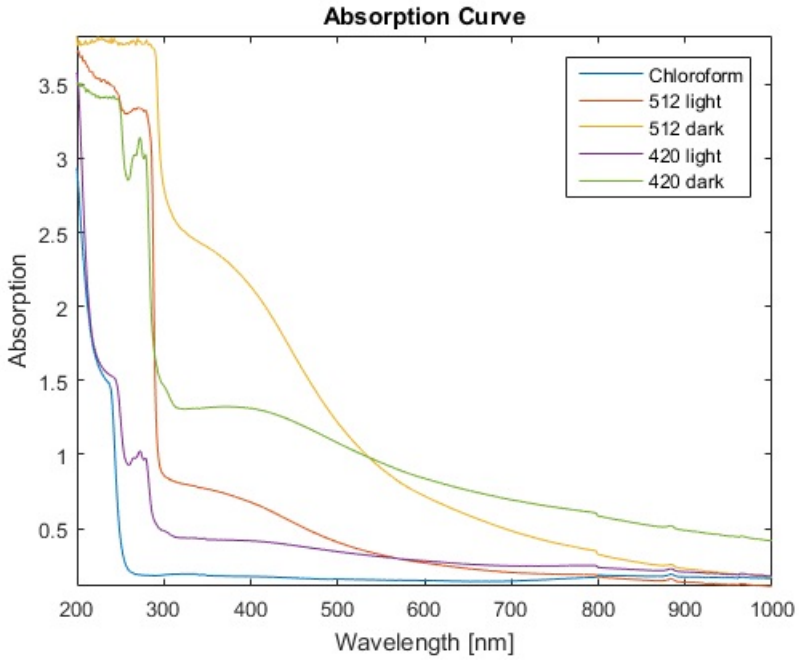

FIGURE 4.4: Absorption curve highlighting the characteristics of the NCs at smaller wavelengths.

in between. The data were saved and can be seen below in Figure 4.5. The detector response was not that of a typical semiconductor where current is minimal until some threshold voltage where it then dramatically increases, but instead the resulting graphic resembled an ohmic relationship characteristic of resistive detector behavior where the applied voltage is linear with respect to current. This is mostly due to inhibited charge transport through the oleic acid ligands which act as an insulating material which the NCs are embedded in.

It can be seen that the detector's bottom contact played a more dominating role on the charge characteristics than the presence or absence of semiconducting polymer MEH-PPV. As expected, the copper bottomed detectors transported much more current than those with the aluminum bottom.

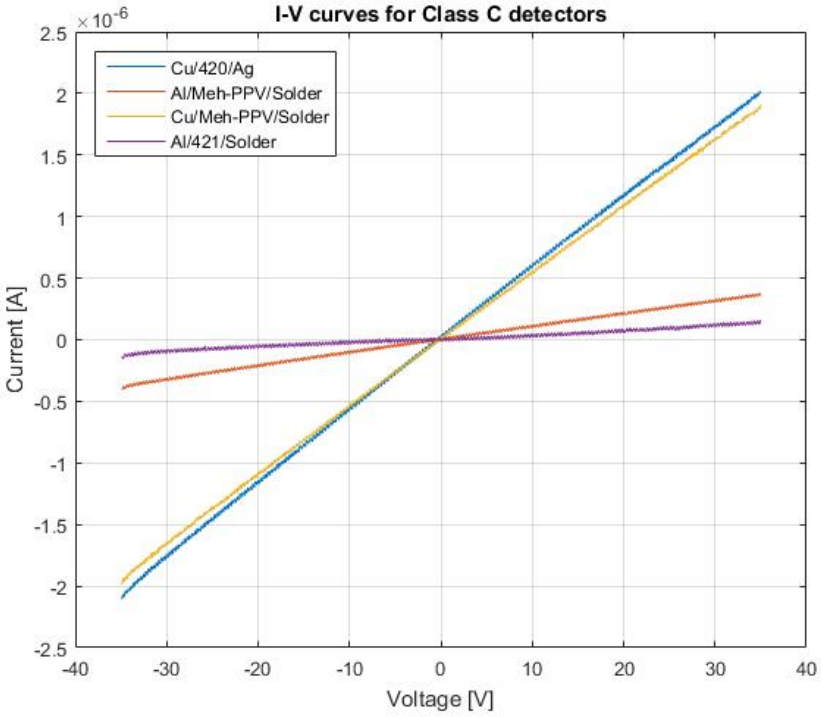

FIGURE 4.5: IV curve for four class C detectors

4.4. Response to Radiation

Detectors were placed inside a small Aluminum box to cut down on environmental noise sources. Wires connecting the electrodes of the detector were connected to wires inside of the box which left the box as a BNC connection as shown in Figure **??**. The BNC output of the detector box was connected to an ORTEC Model 142 preamplifier by means of a BNC to SHV connection. The preamp was powered by a Canberra Model 3106 D High Voltage supply powered by an Ortec 401A NIM bin and its energy output was connected to Channel 1 of a Tektronic TDS 1001 B oscilloscope. A Polonium -210 source was used as it emits a ∼5.3 MeV alpha particle. Although the oscilloscope parameters were varied as well as ranging the high voltage bias on the detector from 0-500 V, it was difficult to discern any signal from noise.

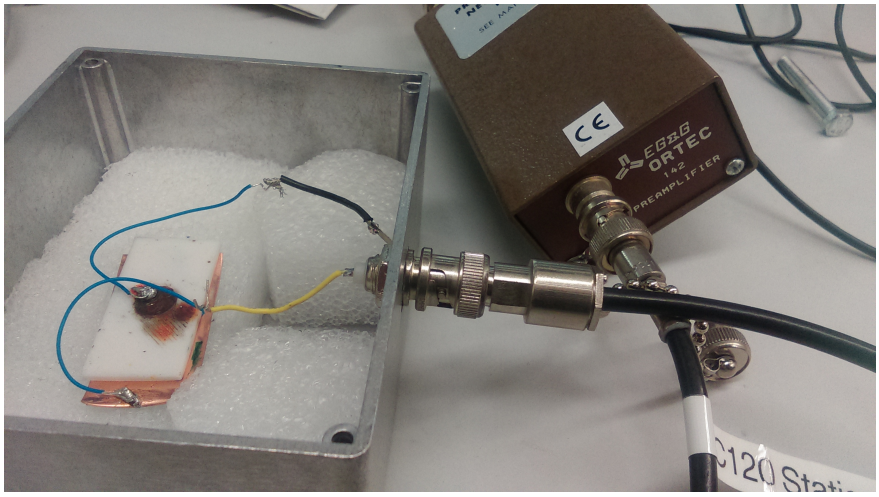

FIGURE 4.6: Mock setup of the detector and preamplifier configuration used in the radiation response testing.

All three class C detectors were unable to repeatedly detect any impinging radiation. This failure to be radiation sensitive is thought to be due to the thickness of the detectors, which by visual inspection, could be as thick as 2 mm. Generally, it is more difficult to extract charge over larger thicknesses due to the enhanced probability of charge carriers to succumb to electronic trapping sites which arise when non-uniform layers of NCs are dried upon each other and become brittle. There were also no significant changes in radiation response from the detectors with blended MEH-PPV NC medium.

5. CONCLUSIONS

In this thesis PbSe NCs capped by oleic acid ligands were successfully prepared via a wet chemical synthesis method. Efforts to deposit them using a layer by layer drop casting method into a radiation sensitive detector however were not as successful, probably in part due to their large thicknesses. The addition of a conductive polymer, MEH-PPV did not substantially improve charge transport as seen in the I-V curves of Section 4.3. nor did they allow for a detector to show a response to radiation. Prototypes have shown the importance of having a reservoir in which to contain the liquid NCs (class A prototypes), as well as the need for reliable, sturdy electrode connections (class D prototypes). Also, an increased amount of metal will be required if an electrode is formed onto the NC by evaporation deposition. Absorption measurements from a Cary 5 spectrophotometer are thought to be an indicator of the presence of NCs as well as the more reliable Transmission Electron Microscope images which can detail the shape, size, and degree of crystalline structure in a small subset of NCs. It is thought that decreasing the thickness of the resulting detector would result in I-V curves resembling semiconductor-like attributes as well as an increased sensitivity towards radiation.

In the near term, thin film detectors can be created while different sizes and shapes of quantum objects are experimented with. Nanowires for example might allow charge to flow more readily than through a matrix filled with insulating ligands. On this note, synthesis methods which employ conductive ligands would be most preferential as ligand exchange techniques which aim to replace the organic ligands with conductive ones can indeed improve charge transport on small scales yet can be detrimental to the uniformity and reliability of a larger solid. If the NCs are made first with the conductive ligands, it is assumed that one could reap the benefits of charge transport without the compromises associated with ligand exchangee.

In the long term, deposition methods need to be improved upon as cracking and drying of individual layers hampers charge transport. If deposition methods can be made such that NC solids can be on the order of centimeters with little charge trapping, the technology will be widely accepted. To this end, one can alter the solvents used along with automation and testing of different deposition methods using different deposition volumes.

BIBLIOGRAPHY

1. Merriam-webster.com, "Definition of RADIATION", 2016. [Online]. Available: http://www.merriam-webster.com/dictionary/radiation.

2. Scienceworld.wolfram.com, "Radiation – from Eric Weisstein's World of Physics", 2016. [Online]. Available: http://scienceworld.wolfram.com/physics/Radiation.html.

3. N. Carron, An introduction to the passage of energetic particles through matter. pp. 136. Boca Raton: Taylor & Francis, 2007.

4. G. Knoll, Radiation detection and measurement. pp 233. New York: Wiley, 2000.

5. S. Luryi, J. Xu and A. Zaslavsky, Future trends in microelectronics. Hoboken, N.J.: IEEE Press, 2010.

6. H. Khlyap, From Semi Classical Semiconductors to Novel Spintronic Devices. Sharjah: Bentham Science Publishers, 2013.

7. J. Farkas, Irradiation for better foods, Trends Food Sci. Technol., vol. 17, no. 4, pp. 148152, 2006.

8. O. Ikotun and S. Lapi, "The rise of metal radionuclides in medical imaging: copper-64, zirconium-89 and yttrium-86", Future Medicinal Chemistry, vol. 3, no. 5, pp. 599-621, 2011.

9. D. M. Schut, G. M. Williams, Jr., S. Arteaga, T. L. Allen, and T. Novet, Nanocrystal sensitized photovoltaics and photodetectors with performance enhanced using ligand engineering, vol. 8035, no. 1, p. 80351B80351B14, 2011.

10. D. Talapin, "PbSe Nanocrystal Solids for n- and p-Channel Thin Film Field-Effect Transistors", Science, vol. 310, no. 5745, pp. 86-89, 2005.

11. I. Robel, V. Subramanian, M. Kuno and P. Kamat, "Quantum Dot Solar Cells. Harvesting Light Energy with CdSe Nanocrystals Molecularly Linked to Mesoscopic TiO 2 Films", J. Am. Chem. Soc., vol. 128, no. 7, pp. 2385-2393, 2006.

12. R. Somers, M. Bawendi and D. Nocera, "CdSe nanocrystal based chem-/bio- sensors", Chemical Society Reviews, vol. 36, no. 4, p. 579, 2007.

13. H. Doyle and T. A. Betley, Colloidal synthesis of nanocrystals and nanocrystal superlattices, vol. 45, no. 1, pp. 4756, 2001.

14. G. Kim, "Nanocrystalline Semiconductor Nuclear Radiation Detectors", Ph.D thesis, University of Michigan, 2013.

15. Jeffery Harbold, "The Electronic and Optical Properties of Colloidal Leadselenide Semiconductor Nanocrystals", Ph.D thesis Cornell University, 2005

16. V. I. Klimov, Nanocrystal quantum dots. Boca Raton: CRC Press, 2nd ed., 2010.

17. J. J. Peterson, L. Huang, C. Delerue, G. Allan, and T. D. Krauss, Uncovering forbidden optical transitions in PbSe nanocrystals, Nano Lett., vol. 7, no. 12, pp. 38273831, 2007.

18. I. Kang and F. W. Wise, Electronic structure and optical properties of PbS and PbSe quantum dots, J. Opt. Soc. Am. B, vol. 14, no. 7, p. 1632, 1997.

19. G. Allan and C. Delerue, Influence of electronic structure and multiexciton spectral density on multiple-exciton generation in semiconductor nanocrystals: Tight-binding calculations, Phys. Rev. B - Condens. Matter Mater. Phys., vol. 77, no. 12, pp. 110, 2008.

20. I. Moreels, K. Lambert, D. De Muynck, F. Vanhaecke, D. Poelman, J. C. Martins, G. Allan, and Z. Hens, Composition and size-dependent extinction coefficient of colloidal PbSe quantum dots, Chem. Mater., vol. 19, no. 25, pp. 61016106, 2007.

21. A. Smith and S. Nie, "Semiconductor Nanocrystals: Structure, Properties, and Band Gap Engineering", Accounts of Chemical Research, vol. 43, no. 2, pp. 190-200, 2010.

22. M. C. Beard, Multiple exciton generation in semiconductor quantum dots, J. Phys. Chem. Lett., vol. 2, no. 11, pp. 12821288, 2011.

23. R. D. Schaller and V. I. Klimov, High efficiency carrier multiplication in PbSe nanocrystals: Implications for solar energy conversion, Phys. Rev. Lett., vol. 92, no. 18, pp. 1866011, 2004.

24. R. J. Ellingson, M. C. Beard, J. C. Johnson, P. Yu, O. I. Micic, A. J. Nozik, A. Shabaev, and A. L. Efros, Highly efficient multiple exciton generation in colloidal PbSe and PbS quantum dots, Nano Lett., vol. 5, no. 5, pp. 865871, 2005.

25. R. D. Schaller, J. M. Pietryga, and V. I. Klimov, Carrier Multiplication in InAs Nanocrystal Quantum Dots with an Onset Defined by the Energy Conservation Limit Carrier Multiplication in InAs Nanocrystal Quantum Dots with an Onset Defined by the Energy Conservation Limit, 2007.

26. R. D. Schaller, M. Sykora, J. M. Pietryga, and V. I. Klimov, Seven excitons at a cost of one: Redefining the limits for conversion efficiency of photons into charge carriers, Nano Lett., vol. 6, no. 3, pp. 424429, 2006.

27. G. Kim, J. Huang and M. Hammig, "An Investigation of Nanocrystalline Semiconductor Assemblies as a Material Basis for Ionizing-Radiation Detectors", IEEE Trans. Nucl. Sci., vol. 56, no. 3, pp. 841-848, 2009.

28. A. Owens and A. Peacock, "Compound semiconductor radiation detectors", Nuclear Instruments and Methods in Physics Research Section A: Accelerators, Spectrometers, Detectors and Associated Equipment, vol. 531, no. 1-2, pp. 18-37, 2004.

29. N. Klassen, V. Kedrov, V. Kurlov, Y. Ossipyan, S. Shmurak, I. Shmyt'ko, G. Strukova, N. Kobelev, E. Kudrenko, O. Krivko, A. Kiselev, A. Bazhenov and T. Fursova, "Advantages and Problems of Nanocrystalline Scintillators", IEEE Trans. Nucl. Sci., vol. 55, no. 3, pp. 1536-1541, 2008.

30. L. Jacobsohn, K. Sprinkle, S. Roberts, C. Kucera, T. James, E. Yukihara, T. DeVol and J. Ballato, "Fluoride Nanoscintillators", Journal of Nanomaterials, vol. 2011, pp. 1-6, 2011.

31. S. Stange, Nanocomposite Scintillators For Neutron Capture Measurements. PhD thesis, University of Michigan, 2011.

32. M. D. Hammig, Nanoscale Methods to Enhance the Detection of Ionizing Radiation, Curr. Top. Ioniz. Radiat. Res., 2012.

33. H. Du, C. Chen, R. Krishnan, T. Krauss, J. Harbold, F. Wise, M. Thomas and J. Silcox, "Optical Properties of Colloidal PbSe Nanocrystals", Nano Letters, vol. 2, no. 11, pp. 1321-1324, 2002.

34. S. Sharma, S. Kohli and A. Rastogi, "Quantum confinement effects of CdTe nanocrystals sequestered in TiO2 matrix: effect of oxygen incorporation", Physica E: Low-dimensional Systems and Nanostructures, vol. 25, no. 4, pp. 554-561, 2005.

35. Ellingson, M. Beard, J. Johnson, P. Yu, O. Micic, A. Nozik, A. Shabaev and A. Efros, "Highly Efficient Multiple Exciton Generation in Colloidal PbSe and PbS Quantum Dots", Nano Letters, vol. 5, no. 5, pp. 865-871, 2005.

36. A. Olkhovets, R. Hsu, A. Lipovskii and F. Wise, "Size-Dependent Temperature Variation of the Energy Gap in Lead-Salt Quantum Dots", Phys. Rev. Lett., vol. 81, no. 16, pp. 3539-3542, 1998.

37. V. LaMer and R. Dinegar, "Theory, Production and Mechanism of Formation of Monodispersed Hydrosols", J. Am. Chem. Soc., vol. 72, no. 11, pp. 4847-4854, 1950.

38. J. Yao, K. Elder, H. Guo and M. Grant, "Theory and simulation of Ostwald ripening", Phys. Rev. B, vol. 47, no. 21, pp. 14110-14125, 1993.

39. T. Tan, S. Selvan, L. Zhao, S. Gao and J. Ying, "Size Control, Shape Evolution, and Silica Coating of Near-Infrared-Emitting PbSe Quantum Dots", Chemistry of Materials, vol. 19, no. 13, pp. 3112-3117, 2007.

40. I. Moreels, B. Fritzinger, J. Martins and Z. Hens, "Surface Chemistry of Colloidal PbSe Nanocrystals", J. Am. Chem. Soc., vol. 130, no. 45, pp. 15081-15086, 2008.

41. C. Murray, C. Kagan and M. Bawendi, "Synthesis and Characterization of Monodisperse Nanocrystals and Close-Packed Nanocrystal Assemblies", Annual Review of Materials Science, vol. 30, no. 1, pp. 545-610, 2000.

42. K. Cho, D. Talapin, W. Gaschler and C. Murray, "Designing PbSe Nanowires and Nanorings through Oriented Attachment of Nanoparticles", J. Am. Chem. Soc., vol. 127, no. 19, pp. 7140-7147, 2005.

43. D. Zherebetskyy, M. Scheele, Y. Zhang, N. Bronstein, C. Thompson, D. Britt, M. Salmeron, P. Alivisatos and L. Wang, "Hydroxylation of the surface of PbS nanocrystals passivated with oleic acid", Science, vol. 344, no. 6190, pp. 1380-1384, 2014.

44. N. Anderson, M. Hendricks, J. Choi and J. Owen, "Ligand Exchange and the Stoichiometry of Metal Chalcogenide Nanocrystals: Spectroscopic Observation of Facile Metal-Carboxylate Displacement and Binding", J. Am. Chem. Soc., vol. 135, no. 49, pp. 18536-18548, 2013.

45. O. Semonin, J. Luther, S. Choi, H. Chen, J. Gao, A. Nozik and M. Beard, "Peak External Photocurrent Quantum Efficiency Exceeding 100% via MEG in a Quantum Dot Solar Cell", Science, vol. 334, no. 6062, pp. 1530-1533, 2011.

46. J. Luther, M. Law, Q. Song, C. Perkins, M. Beard and A. Nozik, "Structural, Optical, and Electrical Properties of Self-Assembled Films of PbSe Nanocrystals Treated with 1,2-Ethanedithiol", ACS Nano, vol. 2, no. 2, pp. 271-280, 2008.

47. X. Jiang, R. Schaller, S. Lee, J. Pietryga, V. Klimov and A. Zakhidov, "PbSe nanocrystal/conducting polymer solar cells with an infrared response to 2 micron", Journal of Materials Research, vol. 22, no. 08, pp. 2204-2210, 2007.

48. E. McKigney, R. Del Sesto, L. Jacobsohn, P. Santi, R. Muenchausen, K. Ott, T. Mark McCleskey, B. Bennett, J. Smith and D. Wayne Cooke, "Nanocomposite scintillators for radiation detection and nuclear spectroscopy", Nuclear Instruments and Methods in Physics Research Section A: Accelerators, Spectrometers, Detectors and Associated Equipment, vol. 579, no. 1, pp. 15-18, 2007.

49. G. Allan and C. Delerue, "Confinement effects in PbSe quantum wells and nanocrystals", Phys. Rev. B, vol. 70, no. 24, 2004.

50. L. Wang, M. Califano, A. Zunger and A. Franceschetti, "Pseudopotential Theory of Auger Processes in CdSe Quantum Dots", Phys. Rev. Lett., vol. 91, no. 5, 2003.

51. I. Moreels, K. Lambert, D. De Muynck, F. Vanhaecke, D. Poelman, J. Martins, G. Allan and Z. Hens, "Composition and Size-Dependent Extinction Coefficient of Colloidal PbSe Quantum Dots", Chemistry of Materials, vol. 19, no. 25, pp. 6101-6106, 2007.

52. W. Lu, J. Fang, Y. Ding and Z. Wang, "Formation of PbSe Nanocrystals: A Growth toward Nanocubes", The Journal of Physical Chemistry B, vol. 109, no. 41, pp. 19219-19222, 2005.

APPENDICES

A APPENDIX 3D Time Independent Schrödinger Equation derivation

To begin, let us consider the time dependent Schrödinger Equation which has a potential energy independent of time.

$$i\hbar\frac{\partial\Psi(x,y,z,t)}{\partial t} = -\frac{\hbar^2}{2m}\nabla^2\Psi(x,y,z,t) + V(x,y,z)\Psi(x,y,z,t) \tag{A.1}$$

Assuming $\Psi(r,t)$ is separable in space and time, that is,

$$\Psi(x,y,z,t) = \psi(x,y,z)\lambda(t) \tag{A.2}$$

plugging this back into A.1

$$\psi(x,y,z)i\hbar\frac{\partial\lambda(t)}{\partial t} = -\lambda(t)\frac{\hbar^2}{2m}\nabla^2\psi(x,y,z) + V(x,y,z)\psi(x,y,z)\lambda(t) \tag{A.3}$$

and dividing A.3 by $\Psi(x,y,z,t) = \psi(x,y,z)\lambda(t)$ yields

$$\frac{i\hbar}{\lambda(t)}\frac{\partial\lambda(t)}{\partial t} = -\frac{\hbar^2}{2m\psi(x,y,z)}\nabla^2\psi(x,y,z) + V(x,y,z) \tag{A.4}$$

Since the left hand side is a function of time and is set equal to the right hand side, a function of space, they must both equal a constant. It is customary to set this constant E, as it will later represent energy. Thus we are left with two equations to solve:

$$i\hbar\frac{\partial\lambda(t)}{\partial t} = E\lambda(t) \tag{A.5}$$

and

$$-\frac{\hbar^2}{2m}\nabla^2\psi(x,y,z) + V(x,y,z)\psi(x,y,z) = E\psi(x,y,z) \tag{A.6}$$

The first, A.5 has the general solution

$$\lambda(t) = C\,\mathrm{e}^{\frac{-iEt}{\hbar}} \tag{A.7}$$

where C is an arbitrary constant.

The second, A.6 is known as the 3D Time Independent Schrödinger Equation. The general solution of the wave function however will have solutions of the form

$$\Psi(x, y, z, t) = \psi(x, y, z)\, \mathrm{e}^{\frac{-iEt}{\hbar}} \tag{A.8}$$

B APPENDIX 3D Particle in a Box derivation

We start with the 3D Time Independent Schrödinger Equation and assume independence of each spacial dimension of both the spacial part of the wavefunction, as well as the time independent potential energy. We will define the potential energy to be zero within the box and infinite at the boundary of the box as well as outside it.

$$V(x,y,z) = \left\{ \begin{array}{ll} 0, & 0 < x_i < L_i \\ \infty, & \text{otherwise} \end{array} \right\} \tag{B.1}$$

We will solve the time independent Schrödinger Equation in each dimension. Since the solution is the same in any dimension we will use indicies to represent either x, y, or z. Further, we solve the equation to find solutions within the box where the potential energy is equal to zero. Thus the equation reduces to

$$-\frac{\hbar^2}{2m}\nabla^2\psi_i = E_i\psi_i \tag{B.2}$$

where the total energy of the three dimensional system $E_{total} = E_x + E_y + E_z$.

We now can rearrange and make the substitution $\kappa_i = \sqrt{\frac{2mE_i}{\hbar^2}}$

$$\frac{\hbar^2}{2m}\nabla^2\psi_i(i) = -\kappa_i^2\psi_i(i) \tag{B.3}$$

Leaving it in the form of a typical second order differential equation with wave solutions

$$\psi_i(i) = A_i sin(\kappa_i i) + B_i cos(\kappa_i i) \tag{B.4}$$

However, with the boundary conditions being that at the walls of the box, $\psi_i(0) = \psi(L_i) = 0$,. The first implies $B_i = 0$ and the second forces

$$\psi_i(i) = A_i sin(\kappa_i L_i) = 0 \tag{B.5}$$

Forcing $\kappa_i = \frac{n_i \pi}{L_i}$ for any integer n_i. However, $\kappa_i = \sqrt{\frac{2mE_i}{\hbar^2}}$ and we find the relation:

$$E_i = \frac{\kappa_i^2 \hbar^2}{2m} = \frac{n^2 \pi^2 \hbar^2}{2mL_i^2} \tag{B.6}$$

Normalizing all the functions and placing them all together we get

$$\psi(x,y,z) = \psi_x(x)\psi_y(y)\psi_z(z) = \sqrt{\frac{8}{L_x L_y L_z}} sin(\kappa_x x) sin(\kappa_y y) sin(\kappa_z z) \tag{B.7}$$

C APPENDIX MCNPX Card

PbSe NC detector: Alpha Source

c cell cards————————————

1 1 -.0012 1 -2 IMP:a=1 $air

2 2 -8.07 -1 IMP:a=1 $ nc

3 0 2 IMP:a=0 $void

c end cell card————————————

c Surface Cards————————————

1 rcc 0 0 1 0 0 1e-1 .75 $NC cylinder vx vy vz (base) hx hy hz (1mm) r

2 so 20 $AIR sphere

c end Surface Card————————————

c Material/Source Cards————————————-

MODE a

PHYS:a

CUT:a j 1e-3

SDEF POS=0 0 -1e-1 ERG=5 vec= 0 0 1 dir=d2 wgt=.5

si2 h 0 .5 1

sp2 d 0 .5 .5

C F2:a 1.3 $ Flux across surface 1 the bottom of the gold

C F12:a 1.2 $ Flux across surface 2 the top of the gold

C F4:a 1 $ alpha flux tally cell 1 (gold)

*F8:a 1 $energy deposition in cell 1 (gold)

E0 .01 100I 5

M1 08000 .2 07000 .8 $ Air- 80 % Nitrogen 20% oxygen

M2 82000 .5 34000 .5 $ simple PbSe

NPS 100000

PRINT 100